Influence of gas radiative property models on Large Eddy Simulation of 1 m methanol pool fires

Fatiha Nmira, Li Ma, Jean-Louis Consalvi

Influence of gas radiative property models on Large Eddy Simulation of 1 m methanol pool fires

Fatiha Nmira[a], Li Ma[a,b], Jean-Louis Consalvi[b,*]

[a] *Direction R&D EDF, 6 Quai Watier, 78401, Chatou Cedex, France*
[b] *Aix-Marseille Université, IUSTI/UMR CNRS 7343, 5 rue E. Fermi, 13453 Marseille Cedex 13, France*

Abstract

The main objective of this work is to analyze the effects of gas radiative property models on the radiative outputs and flame structure in a 1 m diameter methanol pool fire. Large Eddy Simulation (LES) are run with the non-adiabatic steady laminar flamelet (SLF)/presumed filtered density function (FDF) model to close subgrid-scale (SGS) turbulence-chemistry and turbulence-radiation emission interactions. The radiative transfer equation (RTE) is solved using the Finite Volume Method (FVM) with different angular meshes, including uniform angular dicretizations comprising 16 (polar angle) $\times$ 24 (azimuthal angle) and 48 $\times$ 96 control angles and the FT_n scheme with n up to 48. Four gas radiative property models, namely the Rank Correlated Full Spectrum k-distribution (RCFSK), the non-grey Weighted-Sum-of-Grey-Gases (WSGG), and two versions of the grey WSGG based on different evaluations of the mean path length are assessed. Model predictions with the RCFSK reproduce with fidelity the available experimental data in terms of

*Corresponding author
Email addresses: fatiha.nmira@edf.fr (Fatiha Nmira), li.ma@edf.fr (Li Ma), jean-louis.consalvi@univ-amu.fr (Jean-Louis Consalvi)

flame structure and radiative loss to the surrounding. The radiative heat transfer within the flame, where radiation is isotropic, is adequately resolved with the FT_{12} angular resolution whereas finer angular meshes with at least 32 segments to discretize the polar angle are required to predict accurately the vertical distributions of radiative flux outside the flame. The grey models fail to reproduce the radiative structure of the flame, predicting an optically thin flame instead of an optically intermediate medium. In an opposite way, although the non-grey WSGG overestimates both emission and absorption, it provides predictions in overall reasonable agreement with the RCSFK.
Keywords: Large methanol pool fire, large eddy simulation, radiative heat transfer, gas radiative property models, angular discretization.

---

1. Introduction

Experimental studies evidenced that radiation is the dominant mode of heat transfer to fuel surface for scales larger than about 0.2-0.3 m [1]. More quantitatively, Hamins et al. [2] reported that radiation contributes to the total heat feedback for 55 %, 80 %, and 96 % in the case of 0.3 m diameter methanol, heptane and toluene pool fires, respectively. This contribution generally increases with the fire size and the fuel sooting propensity [3]. Consequently, the development of LES-based fire simulators over the last 20 years raised naturally the issue of the radiation modelling for fire applications [4–15]. At the same time, the radiative heat transfer community reported significant progresses in the modelling of radiation in turbulent flames [16]. This issue can be divided into three separate sub-problems, namely the RTE solver, the spectral dependence of radiating species, and the turbulence radiation interaction (TRI). Firstly, nowadays discrete ordinates methods (DOM) and finite volume method (FVM) are widely used as RTE solver mainly due to their compatibility with the discretization of the fluid dynamics equations, ease to code, fairly good accuracy, and often acceptable computational efficiency [17]. Moreover, Monte Carlo techniques were also used in some recent simulations of flames (see [15, 18–20]). Secondly, the absorption coefficient of the radiating combustion gases is strongly dependent on the wavenumber. The modelling of gas radiative properties has benefited of the development of accurate high-temperature high-resolution spectroscopic databases such as HITEMP 2010 [21]. Line-by-Line (LBL) has then emerged as the reference for decoupled radiative heat transfer calculations and was combined to Monte Carlo techniques for coupled simulations [18]. However, LBL/Monte

Carlo calculations are limited to academic configurations. Alternative global gas property models were developed based on the k-distribution concept, such as the Full-Spectrum Correlated-k (FSCK) or the Spectral Line based Weighted-Sum-of-Grey-Gases (SLW). These models were found to provide a good compromise between accuracy and computational efficiency and to be adequate for engineering applications [22–29]. Although having similar features with the Weighted-Sum-of-Grey-Gases (WSGG) model, these methods do not suffer from its limitation, namely its restriction to spatially constant absorption coefficients [16]. FSCK/SLW models can be also applied to mixtures of gases and non-grey soot [30]. In addition, the development of look-up tables has significantly improved their computational efficiency [31–36]. Finally, TRI results from the highly non-linear coupling between turbulent fluctuations in temperature, composition, and radiative intensity [37]. Accounting for TRI requires the modelling of two terms, namely absorption TRI and emission TRI. In LES, the contribution of turbulent fluctuations to TRI is decomposed into resolved-scale fluctuations and SGS fluctuations and only these latter require modelling. A consensus was reached that the SGS absorption TRI is negligible in both luminous and non-luminous flames [19, 38, 39]. On the other hand, the importance of SGS emission TRI was found to depend on the filter size [38, 39] and its modelling is strongly dependent on the turbulent combustion model. An appropriate way to model SGS emission TRI is to consider FDF approaches [19, 40, 41].

One of the objectives of the fire simulators is to forecast the growth of fires at the scale of industrial fires. This introduces considerable challenges for the modelling of the physical processes involved and compromises between

accuracy and computational resources have to be found. Consequently, less sophisticated radiation models were generally considered in most of the LES of fire plumes reported to date. These studies have mainly considered DOM and FVM as RTE solver [4–14]. Since the computational cost related to the solution of the RTE is relatively high, simplified radiative property models, assuming either an optically thin medium with the emission specified to reproduce the measured radiant fraction [4, 5, 10] or a grey medium [6–8, 11, 13], were generally retained. Nevertheless, non-grey radiative property models, based on non-grey versions of the WSGG or box models [12, 14], were also applied in LES of medium-scale methanol and ethanol pool fires. Sivic et al. [14] assessed several radiative property models, including grey and non-grey implementations of the WSGG and the exponential wide band-based box model, to simulate 30 cm diameter methanol pool fires and recommended to use non-grey versions of the WSGG. On the other hand, LES of ethanol pool fires with diameters ranging from 0.5 m to 2 m demonstrated that SGS TRI contributes for a non-negligible part to radiative loss and its contribution increases significantly with the pool size [42]. Neglecting it affects significantly the predictions of the fire plume structure and radiative heat flux even for medium-scale pool fires. Several other works [8, 11, 14] have extended the moment-based closure, proposed by Snegirev for RANS [43], to model SGS emission TRI. This approach consists in approximating the filtered emission term by a Taylor series expansion and retaining only the lower-order moments. Nevertheless, moment-based methods introduce empirical adjustable coefficients that are generally tuned to match the experimental data [8, 11, 14]. Wu et al. presented DNS of a 7.1 cm heptane

pool fire using a very fine description of radiative heat transfer [15]. In their work, radiation was modelled using the LBL/Photon Monte Carlo proposed by Wang et al. [18], and the contributions of CO_2, H_2O, CO, CH_4, C_2H_4 and soot were taken into account.

The objective of the present study is twofold. The first aim is to validate the overall performance of a LES-based fire model to reproduce the structure of the 1 m methanol pool fire studied experimentally by Sung et al. [44]. The model includes a non-adiabatic SLF/presumed FDF model to close SGS turbulence-chemistry and turbulence-radiation emission interactions and the Rank Correlated Full Spectrum k-distribution (RCFSK) as spectral gas radiation model [29]. This fine description of gas radiation and SGS TRI in large-scale methanol pool fires constitutes the main originality of these simulations. The second aim is to assess the effects of angular discretization and radiative property models on radiative heat transfer. Four radiative property models, namely the RCFSK, the non-grey WSGG, and two versions of the grey WSGG based on different evaluations of the mean path length are considered. To the best of the authors knowledge, such a complete analysis of radiative property models on LES of large pool fires was not reported in the literature.

The article is organized as follows. The second section presents the numerical and physical models including the different radiation models. Numerical predictions and effects of the radiation models on flame structure and radiative outputs are discussed in Section 3. Finally Section 4 contains the concluding remarks drawn from the present work.

2. Numerical and physical models

2.1. Governing equations

The turbulent diffusion flame flow field is modelled by the Favre-Filtered conservation equations of mass, momentum, enthalpy, $\tilde{h}$, and mixture fraction, $\tilde{Z}$, as:

$$\frac{\partial \bar{\rho}}{\partial t} + \frac{\partial \bar{\rho}\tilde{u}_i}{\partial x_i} = 0 \tag{1}$$

$$\frac{\partial \bar{\rho}\tilde{u}_j}{\partial t} + \frac{\partial \bar{\rho}\tilde{u}_i\tilde{u}_j}{\partial x_i} = -\frac{\partial \bar{p}}{\partial x_j} + \frac{\partial}{\partial x_i}\left((\tilde{\mu}+\mu_t)\tilde{S}_{ij}\right) + (\bar{\rho}-\rho_\infty)g_j \tag{2}$$

$$\frac{\partial \bar{\rho}\tilde{Z}}{\partial t} + \frac{\partial \bar{\rho}\tilde{u}_i\tilde{Z}}{\partial x_i} = \frac{\partial}{\partial x_i}\left(\bar{\rho}(\tilde{D}+D_t)\frac{\partial \tilde{Z}}{\partial x_i}\right) \tag{3}$$

$$\frac{\partial \bar{\rho}\tilde{h}}{\partial t} + \frac{\partial \bar{\rho}\tilde{u}_i\tilde{h}}{\partial x_i} = \frac{\partial}{\partial x_i}\left(\bar{\rho}(\tilde{D}+D_t)\frac{\partial \tilde{h}}{\partial x_i}\right) - \overline{\nabla \cdot \dot{q}''_R} \tag{4}$$

$\bar{(\cdot)}$ and $\tilde{(\cdot)}$ represent filtered and density-weighted filtered quantities, respectively. ρ, u_i, p, D, μ are the density, velocity vector components, $\mathbf{u} = (u, v, w)$, pressure, molecular diffusivity, and viscosity, respectively.
The SGS momentum stress and scalar flux are computed using a dynamic Smagorinsky model and a dynamic eddy diffusivity model, respectively [45]:

$$\tau^{sgs}_{u_iu_j} = -\bar{\rho}(\widetilde{u_iu_j} - \tilde{u}_i\tilde{u}_j) \approx 2\mu_t\tilde{S}_{ij} \tag{5}$$

$$\tau^{sgs}_{u_iZ} = -\bar{\rho}(\widetilde{u_iZ} - \tilde{u}_i\tilde{Z}) \approx \bar{\rho}D_t\frac{\partial \tilde{Z}}{\partial x_i} \tag{6}$$

where $\mu_t = C_s\bar{\rho}\Delta^2|\tilde{S}|$ is the turbulent eddy viscosity and $\bar{\rho}D_t = C_z\bar{\rho}\Delta^2|\tilde{S}|$ is the SGS diffusivity, with $|\tilde{S}| = \sqrt{2\tilde{S}_{ij}\tilde{S}_{ij}}$ being the norm of the resolved strain rate tensor, $\tilde{S}_{ij}$, and Δ the filter width. The coefficients C_s and C_z are calculated using the dynamic procedures according to Refs. [45, 46].

The Favre-filtered transport equations are solved by using the second-order iterative variable-density solver developed by Ma et al. [47] and implemented in the finite volume code *Code_Saturne* v5.0.9 [48]. The second-order Crank-Nicolson scheme is used for time advancement. The Total Variation Diminuishing (TVD) scheme is applied for convection in the mixture fraction transport to limit numerical oscillation whereas a second-order central difference scheme (CDS) is used for diffusion. For the momentum equation both convective and diffusive terms are discretized by using a second-order CDS.

2.2. Combustion model

The non-adiabatic SLF model is used to obtain the local thermochemical state relationship, ϕ^{fl}, as a function of the mixture fraction, Z, the scalar dissipation rate, χ, and the enthalpy defect, $X_R = h - h_{ad}$, where h_{ad} is the adiabatic enthalpy [49]. The flamelet library was generated by solving the governing equations of counterflow diffusion flames in the physical space at a series of specified strain rates using the CHEMKIN code [50] and the full chemical kinetic mechanism developed by Li et al. [52]. The mixture fraction distributions are obtained by solving a transport equation for the mixture fraction, as suggested by Pitsch and Peters [51]. The Favre-filtered thermochemical quantities are then obtained from the state relationships by convolution with a presumed FDF:

$$\tilde{\phi} = \int \phi^{fl}(Z, \chi, X_R)\tilde{P}(Z, \chi, X_R)dZd\chi dX_R \tag{7}$$

Z, χ and X_R are assumed to be statistically independent and the marginal FDFs are modelled by a β-distribution for Z and two δ-distributions for χ

and X_R:

$$\tilde{P}(Z,\chi,X_R) = \beta(Z;\tilde{Z},V_Z)\delta(\chi-\tilde{\chi})\delta(X_R-\tilde{X}_R) \tag{8}$$

where V_Z is the SGS mixture fraction variance. All thermochemical quantities can then be expressed as a function of $\tilde{Z}, V_Z, \tilde{\chi}$, and $\tilde{X}_R$ [53].

2.3. Subgrid scalar variance and dissipation modelling

In this work, we consider a transport equation for the second moment of the mixture fraction $\widetilde{Z^2}$ (STE) and the subgrid variance is then calculated from its definition [54], $V_Z = \widetilde{Z^2} - \tilde{Z}^2$:

$$\frac{\partial\bar{\rho}\widetilde{Z^2}}{\partial t} + \frac{\partial\bar{\rho}\tilde{u}_i\widetilde{Z^2}}{\partial x_i} = \frac{\partial}{\partial x_i}\left(\bar{\rho}(\tilde{D}+D_t)\frac{\partial\widetilde{Z^2}}{\partial x_i}\right) - \bar{\rho}\tilde{\chi} \tag{9}$$

The remaining modelling step for STE concerns the filtered scalar dissipation rate, $\tilde{\chi}$. Jiménez et al. [54] proposed to model the filtered scalar dissipation rate by relating the SGS scalar mixing time scale to the SGS turbulent time scale. An equivalent SGS turbulent characteristic time $\bar{\tau}$ is introduced as the ratio between SGS kinetic energy, κ^{sgs}, and the filtered kinetic energy dissipation rate, $\tilde{\varepsilon}$. Given a proportionality between both time scales, the model for $\tilde{\chi}$ is derived as:

$$\frac{\tilde{\chi}}{V_Z} = \frac{1}{\tilde{\tau}_Z} \approx \frac{C}{\tilde{\tau}} = C\frac{\tilde{\varepsilon}}{\kappa^{sgs}} \tag{10}$$

Therefore, the filtered scalar dissipation rate $\tilde{\chi}$ can be written as [54] with C_I computed by a dynamic approach:

$$\tilde{\chi} = \frac{\tilde{D}+D_t}{C_I\Delta^2}V_Z \tag{11}$$

2.4. Radiation modelling

Water vapour and carbon dioxide are considered as the only radiating species since our simulations showed that the contribution of carbon monoxide is negligible. For all the gas radiative property models, the line parameters of CO_2 and H_2O are taken from HITEMP 2010 [21]. The filtered RTE can be written in a generic form as follows [16]:

$$\frac{d\overline{I_i}}{ds} + \overline{\kappa_i I_i} = \overline{\kappa_i a_i I_b}; \qquad i = 1, N_g \tag{12}$$

where I_i, κ_i, and I_b are the radiative intensity, non-grey absorption coefficient, and blackbody intensity, respectively. N_g and a_i are the number of quadrature points and the stretching function for the RCFSK or the number of grey gases and the weight factor for the non-grey WSGG, respectively. For the grey models, only one RTE ($N_g = 1$) has to be solved and the weight factor is set equal to 1.

The filtered absorption term, $\overline{\kappa_i I_i}$, is closed by neglecting the SGS absorption TRI, leading to $\overline{\kappa_i I_i} \approx \overline{\kappa_i}\,\overline{I_i}$. This approximation was found to be valid in LES of non-luminous and luminous lab- and large-scale diffusion flames in which about 80% of the turbulent fluctuations are resolved [19, 38, 39]. The absorption coefficient and the emission term depend only on temperature and mole fractions of CO_2 and H_2O. Therefore, the filtering operation for these terms can be performed accurately by using the FDF approach [16]:

$$\overline{\kappa_i} = \bar{\rho} \int \frac{(\kappa_i)^{fl}(Z, \tilde{\chi}, \tilde{\chi}_R)}{\rho^{fl}(Z, \tilde{\chi}, \tilde{\chi}_R)} \beta(Z; \tilde{Z}, V_Z) dZ \tag{13}$$

$$\overline{\kappa_i a_i I_b} = \bar{\rho} \int \frac{(\kappa_i a_i I_b)^{fl}(Z, \tilde{\chi}, \tilde{\chi}_R)}{\rho^{fl}(Z, \tilde{\chi}, \tilde{\chi}_R)} \beta(Z; \tilde{Z}, V_Z) dZ \tag{14}$$

2.4.1. RTE solver

The filtered RTE is solved by using the FVM [55, 56] with a uniform angular mesh of 384 ($N_\theta \times N_\phi = 16 \times 24$) control angles. The subscripts θ and ϕ represent the polar and azimutal angles, respectively. The selection of this angular discretization was based on the study of Jensen et al. [57] who suggested that, for uniform angular discretization, approximately 50 angles inside and 350 angles outside the fire are needed to adequately resolve radiation.

A frozen field analysis will be considered to investigate the angular mesh effects on the radiative outputs. In this analysis, instantaneous fields of filtered absorption coefficient (Eq. (13)) and emission term (Eq. (14)), computed with the uniform 16×24 angular mesh, are saved during the statistically stationary state. These fields are used to solve instantaneous RTE (Eq. (12)) with the other angular meshes over the statistically stationary state and, then, the resulting instantaneous radiative intensities are averaged to get the mean absorption term and radiative fluxes. The other angular meshes considered in the present study are, on the one hand, a three-time finer uniform angular mesh with 4608 ($N_\theta \times N_\phi = 48 \times 96$) control angles and, on the other hand, the non-uniform FT_n angular discretizations [58]. In the FT_n FVM, the polar angle, θ, is divided uniformly into an even number, n, while the azimuthal angle, ϕ, is uniformly divided into the numbers of the sequence of 4, 8, 12,...,$2n-4$, $2n$, $2n$, $2n-4$,..., 8 and 4 in each level of the polar angle

[58]. This results in $n \times (n+2)$ control angles.

Using a frozen field analysis is justified by the fact that meshes finer than 16 $\times$ 24 were found to have no influence on the radiative heat transfer inside the flame and to change only the vertical distributions of radiative flux outside the flame. Refining the angular mesh further than 48 $\times$ 96 was found to have no effect on the vertical distributions of radiative flux outside the flame and this discretization will be used as reference.

2.4.2. RCFSK

The RCFSK model belongs to the family of the global k-distribution-based gas radiation models as the SLW or the classical FSCK. The RCFSK preserves the total emission and does not require any specification of a reference state [29]. In configurations relevant for combustion applications, the RCFSK was found to provide an overall very good agreement with reference LBL or Narrow Band calculations in both emission and absorption dominated problems [29, 59, 60]. Consequently, it will be used as reference in the present study.

Full spectrum (FS) cumulative k-g distribution function is defined as [16, 26]:

$$g(k,\phi,T_p) = \frac{\int_0^\infty H[k-\kappa_\eta(\phi)] I_{b\eta}(T_p) d\eta}{I_b(T_p)} \tag{15}$$

where $\phi = \{x_{CO_2}, x_{H_2O}, T\}$ is an array of thermodynamic variables affecting the spectral absorption coefficient, κ_η, at the wavenumber η. H is the Heaviside function, k a given value of the absorption coefficient, and $I_{b\eta}(T_p)$ the spectral blackbody intensity at the Planck temperature T_p. In the present

study, mixed FS k-g distributions (for mixtures of H_2O and CO_2) are constructed from HITEMP 2010 [21] by using the procedure proposed by Modest and Riazzi [30], and a 10-point Gauss-Legendre quadrature scheme ($N_g = 10$) is used (see Eq. (12)). For each quadrature point, g_i, the RCFSK scheme determines the absorption coefficient, κ_i, and the stretching function, $a_i(T)$, by solving [29]:

$$g(\kappa_i, \phi, T_p) = g_i \tag{16}$$

$$a_i(T) = \frac{g[\kappa_i, \phi, T] - g[\kappa_{i-1}, \phi, T]}{\Delta g}; \qquad \Delta g = g_i - g_{i-1} \tag{17}$$

The divergence of the radiative flux is then computed from the following equation:

$$\nabla \cdot \dot{q}''_R = \underbrace{\sum_{i=1}^{N_g} 4\pi\kappa_i a_i I_b \Delta g}_{\dot{Q}'''_{emi}} - \underbrace{\sum_{i=1}^{N_g} \kappa_i G_i \Delta g}_{\dot{Q}'''_{abs}} \tag{18}$$

where $G_i = \int_{4\pi} I_i d\Omega$ with Ω being the solid angle. As expected, predictions were found insensitive to the choice of T_p. In the present simulations, T_p was set equal to 1500 K.

2.4.3. WSGG

The WSGG assumes that the total emissivity, ϵ, can be computed as follows [16]:

$$\epsilon = \sum_{i=1}^{N_g} a_i(T)[1 - exp(-\kappa_i L)] \tag{19}$$

with

$$\kappa_i = (x_{CO_2} + x_{H_2O}) p_0 \kappa_{p,i} \quad and \quad a_i = \sum_{k=0}^{K} b_{i,k} T^k \tag{20}$$

L is the mean path length. In the present study, $p_0 = 1$ atm, $N_g = 4$ and $K = 4$. The constant WSGG parameters, $\kappa_{p,i}$ and $b_{i,k}$, derived in Ref. [61] for $x_{H_2O}/x_{CO_2} = 2$, are used. These parameters were optimized to fit total emissivities determined from HITEMP 2010 [21] for a set of specified temperatures and optical path-lengths.

The non-grey WSGG solves 4 RTEs ($N_g = 4$). For each RTE, κ_i and a_i are computed from Eq. (20). This approach will be referred to as WSGG-NG, hereafter. The divergence of the radiative flux is then determined as:

$$\nabla \cdot \dot{q}''_R = \underbrace{\sum_{i=1}^{N_g} 4\pi\kappa_i a_i I_b}_{\dot{Q}'''_{emi}} - \underbrace{\sum_{i=1}^{N_g} \kappa_i G_i}_{\dot{Q}'''_{abs}}; \quad with \quad G_i = \int_{4\pi} I_i d\Omega \tag{21}$$

The grey WSGG consists in determining a grey absorption coefficient, κ, from the WSGG emissivity (Eq. 19):

$$\kappa = -\frac{ln(1-\epsilon)}{L} \tag{22}$$

There is no theoretical procedure to determine L in Eqs. (19) and (22). Two approaches were considered in the literature. The first approach consists in using a cell-based mean path length whereas the second assumes a domain or flame-based mean path length. The two options are considered in the present study. The cell-based approach is referred to as WSGG-G-CB hereafter and, following the recommendation of Refs. [62, 63], L is determined as five times the characteristic local grid size. On the other hand, the flame-based determination of L is arbitrary since it depends on the way to define the flame. In the present study, $L = 4V/A$, where V and A are the flame

volume and surface, respectively. The flame shape is assumed to be a cone with a circular base of diameter equal to the pool diameter and a height defined by the iso-contour 600 K. This value was selected since it is expected to characterize the intermittent flame tip [64]. Varying this temperature between 500 and 700 K was found to effect the radiant fraction by less than 1.5 %. This approach will be referred to as WSGG-G-FB, hereafter.

3. Results and discussions

3.1. Computational details

The 1 m diameter methanol pool fire investigated experimentally by Sung et al. [44] is considered for simulations. The burner was located 30 cm above the floor and the fuel lip height, defined as the fuel level below the burner rim, was maintained at 1 cm. The heat release rate (HRR, $\dot{Q}_{ch}$) was determined either from oxygen consumption calorimetry or from the measured mass burning rate assuming a complete combustion. As expected for methanol, both techniques were found to be consistent with a measured HRR of 256 kW. Fast Fourier power spectrum of the time-varying flame height revealed a puffing frequency of 1.37 Hz and a first harmonic of 2.75 Hz. Temperature measurements were performed using 50 μm diameter Type S thermocouples and were corrected for thermal inertia effects. The compensation technique was based on an instantaneous time constant computed from the thermocouple bead geometry and an estimation of the flow conditions for the convective heat transfer. Vertical distribution, at a distance of 2.07 m from the pool axis, and radial distribution, along the plane of the burner rim outside the pool fires, of radiative flux were measured with wide-view angle, water-cooled,

Gardon-type total heat flux gauges (see Fig.1) . Sung et al. [44] also deduced from their data the total radiative feedback, $\dot{Q}_{R,S} = \int_{A_b} \dot{q}''_{R,S} dA$ (see Fig. 1). This quantity represents the incident radiative flux on the fuel surface integrated over the burner surface, A_b. It was normalized by the HRR to provide $\chi_{R,S} = \dot{Q}_{R,S}/\dot{Q}_{ch}$. This latter set of data is completed by the local radiative feedback, $\dot{q}''_{R,S}$, measured by Klassen and Gore [65].

Simulations are performed in a computational domain (x, y, z) of $9 \times 9 \times 7$ m^3 (see Fig. 1). In the present study, z represents the vertical direction. Consistently with the experimental configuration, the burner is located 30 cm above the floor and the fuel lip height is set equal to 1 cm. It was found necessary to respect these experimental features to reproduce adequately the pool dynamics. A non-uniform structured mesh with 8.01 million of cells is considered. The mesh is refined over the fuel surface with a cell size (Δx, Δy, Δz) of $8.15 \times 8.15 \times 5$ mm^3. Outside the pan, Δx and Δy are stretched progressively towards the sides. In the vertical direction, $\Delta z = 5$ mm is applied between the fuel surface (z = 0) and the burner rim (z = 1 cm). Δz is then stretched from z = 0.01 m to z = 0.326 m to reach 1.58 cm. A uniform $\Delta z = 1.58$ cm is then applied up to z = 1.8 m. Above z= 1.8 m, Δz is stretched progressively.

Typical outflow and entrainment boundary conditions are used for open boundaries at the outlet and sides, respectively. The fuel inlet temperature is set to the boiling temperature of methanol, i.e. 338 K. The inlet velocity is imposed to provide the specified HRR and both convective and diffusive mass and energy fluxes are accounted for. In the rest domain, the classical wall boundary condition is imposed.

Simulations were run for 35 s and the time-averaged mean and root mean square values were collected over the last 20 s. The first 15 s of simulation were used to establish a statistically stationary flow. This latter time was selected to correspond to 10 flow-through times, $t_f = \int_0^{L_d} dz/w(0,z)$, based on the centreline velocity along the fire plume, w, and the length of the computational domain, L_d [66]. In addition, it corresponds to more than 20 puffing cycles based on the characteristic puffing frequency of the present pool fire of 1.37 Hz.

All simulations were performed on the supercomputer Gaia of EDF R&D. This cluster is made of 1224 computer nodes and 42912 cores. Processor are Intel Xeon Gold 6140 CPU @ 2.30 GHz. The present LES were performed on 940 cores. Table 1 provides the CPU times for all the radiative models in one time step. A careful examination shows that CPU times for the different angular meshes and the different radiative property models increase almost linearly with number of control angles and the number of RTEs to be solved, respectively.

3.2. Quality of the LES

The ratio of resolved temperature variance, $\langle \widetilde{T'^2} \rangle_{ReS} = \langle \tilde{T}^2 \rangle - \langle \tilde{T} \rangle^2$, to the total temperature variance, $\langle \widetilde{T'^2} \rangle = \langle \widetilde{T^2} \rangle - \langle \tilde{T} \rangle^2$, is considered to assess the quality of the present LES. Figure 2 shows radial profiles of this ratio at different heights above the burner covering the flaming region. It can be observed that more than 80 % of temperature variance is on the whole resolved by the present LES.

Model	Angular mesh	CPU (s)
RCFSK	16×24	247
	48×96	1333
	FT_{12}	200
	FT_{16}	216
	FT_{24}	282
	FT_{32}	375
	FT_{48}	636
RCFSK	48×96	1333
WSGG-NG	48×96	523
WSGG-G-CB	48×96	241
WSGG-G-FB	48×96	230

Table 1: CPU times for different radiative property models and angular meshes.

3.3. Comparison with available experimental data

In this section, the LES results obtained by the RCFSK/FVM (16×24) radiation model are compared with the experimental data.

Figure 3a shows the Power Spectrum Density (PSD) computed with a fast Fourier transform of the times series of the axial velocity along the axis at a height of 0.6 m. The model predicts a puffing frequency of 1.25 Hz and a first harmonic of 2.50 Hz in good accordance with the experimental ones of 1.37 Hz and 2.75 Hz, respectively.

Figure 4a shows the axial distribution of mean temperature. The experimental data exhibit the expected trends. The mean temperature increases with z close to the burner, reaches a plateau in the continuous flame and, then, decreases as z is further increased in the intermittent flame and in the

inert plume. Model predictions are in close agreement with the experimental data in all the flame regions. Figure 4b-f displays also the radial profiles of mean temperature at different heights above the burner. A very good overall agreement is also observed between the model and the experiments.

Figure 5 displays the axial profile and the radial profiles at different heights of the rms values of temperature fluctuations. Figure 5a shows that the measured axial temperature fluctuation is of the order of 290 K very close to the burner and decreases down to 247 K at about z= 0.30 m. After this location, it increases with z to reach a peak of about 330 K at z= 0.8 m before decreasing as z is further increased. The numerical model captures well these trends. In particular, the peak location as well as the rates of increase and decrease are well reproduced. Figure 5 shows also that the experimental data exhibit pronounced M-shaped radial profiles close to the burner and transit progressively toward flatter profiles as z increases (see fig. 5b-f). The model captures also well these trends and provides predictions in overall good agreement with the experimental data. Nevertheless, it overestimates on the whole the temperature fluctuations. These discrepancies may be attributed, at least partially, to the measurements since previous experimental studies suggested that temperature fluctuations may be underestimated when measured by 50 μm thermocouples despite the use of compensation techniques [67–69].

Table 2 reports the total emission, $\dot{Q}_{emi} = \int_V \dot{Q}'''_{emi} dV$, the total absorption, $\dot{Q}_{abs} = \int_V \dot{Q}'''_{abs} dV$, the ratio of $\dot{Q}_{abs}$ to $\dot{Q}_{emi}$ that represents the part of emission reabsorbed within the flame and can be used to quantify the flame

optical thickness [42], the radiant fraction, $\chi_R = (\dot{Q}_{emi} - \dot{Q}_{abs})/\dot{Q}_{ch}$, and $\chi_{R,S}$. These results show that about 59.8 % of emission is reabsorbed within the flame. The predicted χ_R is 0.269 and overestimates the experimental one of 0.22 ± 16 % by about 22 %. The predicted $\chi_{R,S}$ is 0.059, in closer agreement with the experimental data of 0.055 ± 21 %.

Model	Angular mesh	$\dot{Q}_{emi}$ (kW)	$\dot{Q}_{abs}$ (kW)	$\dot{Q}_{abs}/\dot{Q}_{emi}$	χ_R	$\chi_{R,S}$
RCFSK	16 × 24	172	102.6	0.598	0.269	0.059
RCFSK	48 × 96	172	102.6	0.598	0.269	0.059

Table 2: Integrated flame radiative properties. Measured radiant fractions, χ_R, and fractional radiative heat feedback toward the fuel surface, $\chi_{R,S}$, were 0.22 ± 16 % and 0.055 ± 21 %, respectively [44].

The vertical, radial and feedback distributions of radiative flux are plotted in Fig. 6a-c. Let us start to analyze the results obtained with the 16×24 angular discretization. Predictions of the radiative flux in the downward direction outside the burner (see Fig. 6b) and the radiative feedback toward the fuel surface (see Fig. 6c) are in overall good agreement with the experimental data. Nevertheless, the model overpredicts the radiative flux at vicinity of the burner (see Fig. 6b) and underpredicts the radiative feedback by about 10% (see Fig. 6c). On the other hand, the vertical distribution of radiative flux exhibits clearly ray effects, especially for $0 \leq z \leq 1$ m (see Fig. 6a). Such effects are a major drawback of both DOM and FVM and are favored in optically thin medium [17]. As a consequence, the present configuration is particularly sensitive to ray effetcts since radiation travels mainly a transparent medium before reaching the location r = 2.07 m where the vertical

distribution is measured. The ray effects can be reduced by refining the angular mesh [17].

Radiation calculations were also performed by neglecting TRI with the 16 $\times$ 24 angular mesh. In these calculations, radiation is solved in decoupled manner by using time-averaged temperature and mole fractions of CO_2 and H_2O obtained from the LES simulations. The total emission and the radiant fraction, obtained by neglecting TRI, were found to be $\dot{Q}_{emi,NoTRI}$ =40 $\times 10^3$ kW and $\chi_{R,NoTRI} = 0.051$, respectively. A comparison with the predictions reported in Table 2 shows that TRI represents about 80 % of the total emission and radiative loss. This high contribution agrees with the results reported in the literature for medium-scale non-luminous pool fires [12, 42] and can be explained, on the one hand, by the rather low time-averaged temperature in pool fires and, on the other hand, by the high level of turbulence intensity due to the puffing process.

3.4. Effects of angular mesh

Results in Table 2 and Fig. 6a-c show that using the uniform 48 $\times$ 96 angular mesh instead of the uniform 16 $\times$ 24 angular discretization does not modify the predictions of $\dot{Q}_{abs}$, χ_R and $\chi_{R,S}$ as well as the radiative feedback toward the fuel surface (see Fig. 6c). In addition, this has almost imperceptible effects on the radial distribution of radiative flux along the plane of the burner rim (see Fig. 6b). In an opposite way, it improves significantly the vertical distribution of radiative flux by eliminating the ray effects (see Fig. 6a).
Table 3 and Fig. 6d-f investigate the effects of the FT_n angular discretizations on both integrated and local radiative outputs. In agreement with the

previous discussion, the results show clearly that the angular meshes affect only the vertical distribution of radiative flux outside the flame.

Figure 6d shows that significant ray effects are observed for FT_{12} and FT_{16}. The FT_{16} and 16×24 angular meshes have the same polar discretization and differ from the azimuthal discretization. These two angular meshes provide almost identical vertical distributions, showing that the discretization of the polar angle is mainly responsible for these ray effects. This can be explained by the statistically axisymmetric nature of the present fire plume. The FT_{24} angular discretization mitigates the ray effects and predicts the peak of vertical flux within 7 % of the 48×96 angular mesh. However, relative errors as large as about 16 % are still observed at z = 1.2 m. Acceptable predictions of the vertical distribution of radiative flux are observed for the FT_{32} angular discretization, which involves 1088 control angles. The FT_{48} angular discretization provides the same vertical distribution of radiative flux as the uniform 48×96 angular mesh, but considers 2400 control angles instead of 4608.

3.5. Effects of radiative property models

Table 4 shows that the WSGG-NG overestimates significantly both the total emission and the total absorption and, by a less extent, the ratio $\dot{Q}_{abs}/\dot{Q}_{emi}$, the radiant fraction, χ_R, and the normalized radiative feedback to the fuel surface, $\chi_{R,S}$. In particular, these three latter quantities are moderately overestimated by about 8.07 %, 7.03% and 2.10 %, respectively. The WSGG-G-CB and WSGG-G-FB underestimate significantly both the total emission and the total absorption as well as $\dot{Q}_{abs}/\dot{Q}_{emi}$ that is only of about 17.5%

Model	Angular mesh	$\dot{Q}_{emi}$ (kW)	$\dot{Q}_{abs}$ (kW)	$\dot{Q}_{abs}/\dot{Q}_{emi}$	χ_R	$\chi_{R,S}$
RCFSK	48×96	172	102.6	0.598	0.269	0.0587
RCFSK	FT_{12}	172	103.2	0.602	0.267	0.0586
		(0.0)	(0.6)	(0.67)	(-0.74)	(-0.17)
RCFSK	FT_{16}	172	102.6	0.598	0.269	0.0587
		(0.0)	(0.0)	(0.0)	(0.0)	(0.0)

Table 3: Effects of FT_n FVM angular discretization on the integrated flame radiative properties. Values in parenthesis represent the relative errors in % of the current model as compared to the RCFSK/FVM 48×96. Results with FT_n angular discretization higher than n = 16 are not reported since these angular meshes do not introduce any discrepancies on these quantities.

and 9.2 % for the WSGG-G-CB and WSGG-G-FB, respectively, instead of 59.8% for the RCFSK. These results show that the grey models are not able to reproduce the radiative structure of the flame, predicting an optically-thin flame instead of an optically intermediate medium.

The WSGG-G-CB overpredicts χ_R and $\chi_{R,S}$ by 36.4% and 32.9%, respectively. On the other hand, as observed in previous studies involving decoupled radiative heat transfer calculations [12, 70], the WSGG-G-FB provides better predictions of the radiative loss than the WSGG-G-CB. Nevertheless, discrepancies of the order of 18.2 % are still observed for $\chi_{R,S}$.

Figure 7 illustrates the effects of the radiative property models on the radiative flux distributions. Predictions with the WSGG-NG agree well with the RCFSK. On the other hand, the WSGG-G-CB model overpredicts notably these fluxes whereas the WSGG-G-FB underpredicts them but by a less extent. Quantitatively, Fig. 7 shows that the WSGG-G-CB and WSGG-G-FB

Model	Angular mesh	$\dot{Q}_{emi}$ (kW)	$\dot{Q}_{abs}$ (kW)	$\dot{Q}_{abs}/\dot{Q}_{emi}$	χ_R	$\chi_{R,S}$
RCFSK	48 × 96	172	103	0.598	0.269	0.0587
WSGG-NG	48 × 96	209 (21.5)	135 (31.1)	0.646 (8.07)	0.288 (7.06)	0.0600 (1.86)
WSGG-G-CB	48 × 96	114 (-33.7)	19.9 (-80.7)	0.175 (-70.7)	0.367 (36.4)	0.078 (32.9)
WSGG-G-FB	48 × 96	72.5 (-57.8)	6.69 (-93.5)	0.092 (-84.5)	0.257 (-4.46)	0.048 (-18.2)

Table 4: Effects of the gas radiative property models on the integrated flame radiative properties. Values in parenthesis represent the relative errors in % of the current model as compared to the RCFSK/FVM 48 × 96.

lead to relative errors as compared to the RCFSK on the peak of vertical radiative flux (see Fig. 7a), on the radiative flux downward at r = 0.5 m (see Fig. 7b), and on the radiative feedback at the center of the fuel surface (see Fig. 7c), of 15.44 % and -22.05%, 18.95 % and -19.91%, and 40.2 % and -13.97 %, respectively.

The effects of the radiative property models on axial profiles of the mean emission term, mean absorption term, mean divergence of the radiative flux, and mean and rms temperature are investigated in Fig. 8. Consistently with the results in Table 4, the WSGG-NG overestimates significantly both local emission and absorption terms, but predicts a mean radiative source term in much better agreement with the RCSFK. However, the WSGG-NG produces noticeable discrepancies on the mean temperature, especially in the region located between z = 0 and z = 0.75 m. The peak of mean temperature is

slightly shifted toward the fuel surface and its value is underpredicted by about 60 K as compared to the RCFSK. The WSGG-NG model leads also to a slight overprediction of the rms value of temperature fluctuations in this region with a peak value higher by about 20 K than that predicted with the RCFSK. The WSGG-G-CB overestimates substantially the radiative loss (see Fig. 8c). Consequently, it predicts mean temperature significantly lower than the RCFSK along the entire centreline (see Fig. 8d). Figure 8d shows that the peak value of mean temperature is lower by about 150 K than that computed with the RCFSK. A consequence of this underestimation of the temperature is that the buoyant forces are underestimated, producing in turn an underestimation of the temperature fluctuations as observed in Fig. 8e. The WSGG-G-FB model provides a divergence of the radiative flux as well as mean and rms temperature comparable to those predicted by the WSGG-NG model. Nevertheless, it has to keep in mind that the WSGG-NG outperforms significantly the WSGG-G-FB in the prediction of the radiative flux (see Fig. 7).

Eventually, Fig. 3 shows that the gas radiative models have no effect on the prediction of the puffing frequency as well as on the first harmonic.

4. Conclusions

LES of 1 m methanol pool fires have been exercised in order to investigate the effects of gas radiative property models on the radiative outputs and flame structure. The baseline radiation model involves the RCFSK coupled to the FVM with 16×24 control angles. Three other gas radiative property models, namely the WSGG-NG, the WSGG-G-CB and the WSGG-G-FB, are

also considered. In addition, solutions obtained with other angular meshes, including the uniform 48 $\times$ 96 angular discretization and the FT_n scheme with n up to 48, are assessed. The following conclusions can be drawn:

1. The present LES-based fire model involving the non-adiabatic/presumed FDF and RCFSK radiation model provides high fidelity predictions in terms of puffing frequency and first harmonic, mean and fluctuating temperatures, radiative feedback to the pool surface and radiative loss to the surrounding.

2. All radiative outputs at the exception of vertical distributions of radiative flux outside the flame can be accurately predicted with the FT_{12} angular discretization. On the other hand, finer angular meshes, considering at least 32 segments to discretize the polar angle, are required to compute accurately the vertical distributions of radiative flux outside the flame.

3. Whatever the definition of the mean path length, the grey WSGG models fails to reproduce the radiative structure of the fire plume, predicting an optically thin flame instead of an optically intermediate medium. The WSGG-G-FB provides a better description of the radiative loss than the WSGG-G-CB. However, it leads to relative errors in the range 15-20 % on the radiative fluxes.

4. The non-grey WSGG model overestimates significantly both emission and absorption, but leads to predictions of the radiative loss and radiative flux within 10 % of the RCFSK. These results suggest that it can be a reasonable alternative for non-sooting pool fires.

Acknowledgements

JLC wishes to express his gratitude to Electricité de France (EDF) for financial supports.

References

[1] J. de Ris, Fire radiation - A review, Symp. (Int.) Combust., (1979) 1003–1016.

[2] A. Hamins, S.J. Fischer, T. Kashiwagi, M.E. Klassen, J.P. Gore, Heat feedback to the fuel surface in pool fires, Combust. Sci. Technol., 97 (1994) 37–62.

[3] B.B. Ditch, J.L. de Ris, T.K. Blanchat, M. Chaos, R.G. Bill Jr, S.B. Dorofeev, Pool fires - An empirical correlation, Combust. flame, 160 (2013) 2964–2974.

[4] Y. Xi, J.P. Gore, K.B. McGrattan, R.G. Rehm, H.R. Baum, Fire dynamics simulation of a turbulent buoyant flame using a mixture-fraction-based combustion model, Combust. Flame, 141 (2005) 329–335.

[5] Y. Wang, P. Chatterjee, J.L. de Ris, Large Eddy Simulation of fire plumes, Proc. Combust. Inst., 33 (2011) 2473–2480.

[6] Z. Chen, J. Wen, B. Xu, S. Dembele, Large Eddy Simulation of a medium-scale methanol pool fire using the extended eddy dissipation concept, Int. J. Heat Mass Transf., 70 (2014) 389–408.

[7] Z. Chen, J. Wen, B. Xu, S. Dembele, Extension of the eddy dissipation concept and smoke point soot model to the LES frame for fire simulations, Fire Safety J., 64 (2014) 12–26.

[8] P. Chatterjee, Y. Wang, K.V. Meredith, S.B. Dorofeev, Application of

a subgrid soot radiation model in the numerical simulation of a heptane pool fire, Proc. Combust. Inst., 35 (2015) 2573–2580.

[9] G. Maragkos, T. Beji, B. Merci, Advances in modelling in CFD simulations of turbulent gaseous pool fires, Combust. Flame, 181 (2017) 22–38.

[10] G. Maragkos, T. Beji, B. Merci, Large eddy simulations of CH_4 fire plumes, Flow Turb. Combust., 99 (2017) 239–278.

[11] A. Snegirev, E. Markus, E. Kuznetsov, J. Harris, T. Wu, On soot and radiation modeling in buoyant turbulent diffusion flames, Heat Mass Transf. 54 (2018) 2275–2293.

[12] G.C. Fraga, F.R. Centeno, A.P. Petry, P.J. Coelho, F.H.R. França, On the individual importance of temperature and concentration fluctuations in the turbulence-radiation interaction in pool fires, Int. J. Heat Mass Transf., 136 (2019) 1079–1089.

[13] G. Maragkos, T. Beji, B. Merci, Towards predictive simulations of gaseous pool fires, Proc. Combust. Inst., 37 (2019) 3927–3934.

[14] I. Sikic, S. Dembele, J. Wen, Non-grey radiative heat transfer modelling in LES-CFD simulated methanol pool fires, J. Quant. Spectrosc. Radiat. Transf., 234 (2019) 78–89.

[15] B. Wu, S.P. Roy, X. Zhao, Detailed modeling of a small-scale turbulent pool fire, Combust. Flame, 214 (2020) 234–237.

[16] M.F. Modest, D.C. Haworth, Radiative Heat Transfer in Turbulent Combustion Systems: Theory and Applications, Springer, New York, 2016.

[17] P.J. Coelho, Advances in the discrete ordinates and finite volume methods for the solution of radiative heat transfer problems in participating media, J. Quant. Spectrosc. Rad. Transf., 145 (2014) 121–146.

[18] A. Wang, M.F. Modest, D.C. Haworth, Monte Carlo simulation of radiative heat transfer and turbulence interactions in methane/air jet flames, J. Quant. Spectrosc. Rad. Transf., 109 (2008) 269–279.

[19] A. Gupta, D.C. Haworth, M.F. Modest, Turbulence-radiation interactions in Large Eddy Simulations of luminous and nonluminous nonpremixed flames, Proc. Combust. Inst., 34 (2013) 1281–1288.

[20] P. Rodrigues, O. Gicquel, B. Franzelli, N. Darabiha, R. Vicquelin, Analysis of radiative transfer in a turbulent sooting jet flame using a Monte Carlo method coupled to Large Eddy Simulation, J. Quant. Spectrosc. Rad. Transf., 235 (2019) 187–203.

[21] L.S. Rothman, I.E. Gordon, R.J. Barber, H. Dothe, R.R. Gamache, A. Goldman, V.I. Perevalov, S.A. Tashkun, J. Tennyson, HITEMP: the high-temperature molecular spectroscopic database, J. Quant. Spectrosc. Radiat. Transf., 111 (2010) 2139–2150.

[22] M.K. Denison, B.W. Webb, A spectral line based weighted-sum-of-gray-gases model for arbitrary RTE solvers, J. Heat Transf., 115 (1993) 1004–1012.

[23] M.K. Denison, B.W. Webb, The spectral-line-based weighted-sum-of-gray-gases model in nonisothermal nonhomogeneous media, J. Heat Transf., 117 (1995) 359–365.

[24] M.K. Denison, B.W. Webb, Development and application of an absorption line black-body distribution function for CO_2, Int. J. Heat Mass Transf., 38 (1995) 1813–1821.

[25] M.K. Denison, B.W. Webb, The spectral-line weighted-sum-of-gray-gases model for H_2O/CO_2 mixtures, J. Heat Transf., 117 (1995) 788–792.

[26] M.F. Modest, H. Zhang, The full spectrum correlated-k distribution for thermal radiation from molecular gas particulate mixtures, J. Heat Transf., 124 (2002) 30–38.

[27] J. Cai, M.F. Modest, Improved full-spectrum k-distribution implementation for inhomogeneous media using a narrow-band database, J. Quant. Spectrosc. Radiat. Transf., 141 (2014) 65–72.

[28] V.P. Solovjov, F. Andre, D. Lemonnier, B.W. Webb, The rank correlated SLW model of gas radiation in non- uniform media, J. Quant. Spectrosc. Radiat. Transf., 197 (2017) 26–44.

[29] V.P. Solovjov, B.W. Webb, F. Andre, The rank correlated FSK model for prediction of gas radiation in non-uniform media, and its relationship to the rank correlated SLW model, J. Quant. Spectrosc. Radiat. Transf., 214 (2018) 120–132.

[30] M.F. Modest, R.J. Riazzi, Assembly full spectrum k-distribution from a narrow band database: effects of mixing gases, gases and non-gray

absorpting particles and non-gray scatters in non-gray enclosures, J. Quant. Spectrosc. Radiat. Transf., 90 (2005) 169–189.

[31] J.T. Pearson, B.W. Webb, V.P. Solovjov, J. Ma, Efficient representation of the absorption line blackbody distribution function for H_2O, CO_2 and CO at variable temperature, mole fraction, and total pressure, J. Quant. Spectrosc. Radiat. Transf., 138 (2014) 82–96.

[32] C. Wang, M.F. Modest, B. He, Improvement of full-spectrum k-distribution method using quadrature transformation, Int. J. Thermal Sci., 108 (2016) 100–107.

[33] C. Wang, W. Ge, M.F. Modest, B. He, A full-spectrum k-distribution look-up table for radiative transfer in nonhomogeneous gaseous media, J. Quant. Spectrosc. Radiat. Transf., 168 (2016) 46–56.

[34] C. Wang, W. Ge, M.F. Modest, B. He, Full-spectrum k-distribution look-up table for nonhomogeneous gas soot mixtures, J. Quant. Spectrosc. Radiat. Transf., 176 (2016) 129–136.

[35] C. Wang, B. He, M.F. Modest, T. Ren, Efficient full-spectrum correlated-k distribution look-up table, J. Quant. Spectrosc. Radiat. Transf., 219 (2018) 108–116.

[36] C. Wang, B. He, M.F. Modest, Full-spectrum correlated-k-distribution look-up table for radiative transfer in nonhomogeneous participating media with gas-particle mixtures, Int. J. Heat Mass Transf., 137 (2019) 1053–1063.

[37] P.J. Coelho, Numerical simulation of the interaction between turbulence and radiation in reactive flows, Prog. Ener. Combust. Sci., 33 (2007) 311–383.

[38] P.J. Coelho, Approximate solutions of the filtered radiative transfer equation in Large Eddy Simulations of turbulent reactive flows, Combust. Flame, 156 (2009) 1099–1110.

[39] J.L. Consalvi, F. Nmira, W. Kong, On the modeling of the filtered radiative transfer equation in Large Eddy Simulations of lab-scale sooting turbulent diffusion flames, J. Quant. Spectrosc. Radiat. Transf., 221 (2018) 51–60.

[40] F.C. Miranda, P.J. Coelho, F. di Mare, J. Janicka, Study of turbulence-radiation interactions in Large Eddy Simulation of scaled Sandia flame D, J. Quant. Spectrosc. Radiat. Transf., 228 (2019) 47–56.

[41] F.C. Miranda, P.J. Coelho, J. Strölhe, J. Janicka, Large Eddy Simulation of a bluff-body stabilised nonpremixed flame with radiation heat transfer, Combust. Theory and Modelling, (2020), https://doi.org/10.1080/13647830.2020.1727017.

[42] F. Nmira, L. Ma, J.L. Consalvi, Turbulence-radiation interaction in Large Eddy Simulation of non-luminous pool fires, Accepted for presentation at the 38th Symp. Combust., (2020).

[43] Y.A. Snegirev, Statistical modeling of thermal radiation transfer in buoyant turbulent diffusion flames, Combust. Flame, 136 (2004) 51–71.

[44] K. Sung, J. Chen, M. Bundy, M. Fernandez, A. Hamins, The Thermal Character of a 1 m Methanol Pool Fire, NIST Technical Note 2083, 2020.

[45] P. Moin, K. Squires, W. Cabot, S. Lee, A dynamic subgrid-scale model for compressible turbulence and scalar transport, Phys. Fluids A, 3 (1991) 2746–2757.

[46] D.K. Lilly, A proposed modification of the Germano subgrid-scale closure method, Phys. Fluids A, 4 (1992) 633–635.

[47] L. Ma, F. Nmira, J.L. Consalvi, Verification and validation of a variableâdensity solver for fire safety applications, Numer. Heat Transf., Part B:Fund., 76 (2019) 107–129.

[48] Code_Saturne, `http://www.code-saturne.org`.

[49] D. Carbonell, C.D. Perez-Segarra, P.J. Coelho, A. Oliva, Flamelet mathematical models for non-premixed laminar combustion, Combust. Flame, 156 (2009) 334–347.

[50] A.E. Lutz, R.J. Kee, J.F. Grcar, F.M. Rupley, OPPDIF: a FORTRAN program for computing opposed-flow diffusion flames, SAN96-824, Sandia National Laboratories, Albuquerque, NM, USA, 1996.

[51] H. Pitsch, N. Peters, A consistent flamelet formulation for non-premixed combustion considering differential diffusion effects, Combust. Flame, 114 (1998) 26–40.

[52] J. Li, Z. Zhao, A. Kazakov, M. Chaos, F.L. Dryer, J.J. Scire Jr., A comprehensive kinetic mechanism for CO, CH_2O, and CH_3OH combustion, Int. J. Chem. Kinetics, 39 (2007) 109–136.

[53] C.D. Pierce, P. Moin, Progress-variable approach for Large Eddy Simulation of non-premixed turbulent combustion, J. Fluid Mech., 504 (2004) 73–97.

[54] C. Jiménez, F. Ducros, B. Cuenot, B. Bédat, Subgrid scale variance and dissipation of a scalar field in Large Eddy Simulations, Phys. Fluids, 13 (2001) 1748–1754.

[55] G.D. Raithby, E.H. Chui, Finite-volume method for predicting a radiant heat transfer in enclosures with participating media, J. Heat Transf., 112 (1990) 415–423.

[56] J.C. Chai, H.S. Lee, S.V. Patankar Finite volume method for radiation heat transfer, J. Thermophys. Heat Transf., 8 (1990) 419–425.

[57] K.A. Jensen, J.F. Ripoll, A.A. Wray, D. Joseph, M. El Hafi, On various modeling approaches to radiative heat transfer in pool fires, Combust. Flame, 148 (2007) 263–279.

[58] S.H. Kim, K.Y. Huh, A new angular discretization scheme of the finite volume method for 3-D radiative heat transfer in absorbing, emitting and anisotropically scattering media, Int. J. Heat Mass Transf., 43 (2000) 1233–1242.

[59] Y. Liu, G. Liu, F. Liu, J.L. Consalvi, Effects of the k-value solution schemes on radiation heat transfer modelling in oxy-fuel flames using the

full-spectrum correlated k-distribution method, App. Therm. Energy, 170 (2020) 114986.

[60] J.L. Consalvi, F. Andre, F. Coelho, F. França, F. Nmira, M. Galtier, V. Solovjov, B. Webb, Assessment of engineering gas radiative property models in high pressure turbulent diffusion flames, RAD 19, 2019.

[61] F.R. Coelho, F.H.R. França, WSGG correlations based on HITEMP2010 for gas mixtures of H_2O and CO_2 in high total pressure conditions, J. Heat Mass Transf., 127 (2018) 105–114.

[62] G.C. Fraga, L. Zannoni, F.R. Centeno, F.H.R. França, Evaluation of different gray gas formulations against line-by-line calculations in two- and three-dimensional configurations for participating media composed by CO_2, H_2O and soot, Fire Safety J., 108 (2019) 102843.

[63] K. McGrattan, S. Hostikka, R. McDermott, J. Floyd, C. Weinschenk, K. Overholt, Dynamics Simulator Technical Reference Guide Volume 1: Mathematical model, NIST Special Publication 1018 6th Edition, 2014.

[64] B.J. McCaffrey, Purely Buoyant Diffusion Flames Some Experimental Results, NBSIR 79-1910, NIST, 1979

[65] M. Klassen, J.P. Gore, Structure and radiation properties of pool fires, NIST-GCR-94-651, NIST, 1992.

[66] K. Kemenov, H. Wang, S. Pope, Modelling effects of subgrid-scale mixture fraction variance in LES of a piloted diffusion flame, Combust. Theory Mod., 16 (2012) 611-638.

[67] N.L. Crauford, S.K. Liew, J.B. Moss, Experimental and numerical simulation of a buoyant fire, Combust. Flame, 31 (1985) 63–77.

[68] E.J. Weckman, A. Sobiesiak, Processing effects in simultaneous velocity and temperature measurements in an intermittent combusting flow, NATO/ASI on Instrumentation for Combustion and Flow in Engines, 1987.

[69] E.J. Weckman, A.B. Strong, Experimental investigation of the turbulence structure of medium-scale methanol pool fires, Combust. Flame, 27 (1996) 87–88.

[70] R. Demarco, J. Consalvi, A. Fuentes, S. Melis, Assessment of radiative property models in non-gray sooting media, Int. J. Thermal Sci., 50 (2011) 1672–1684.

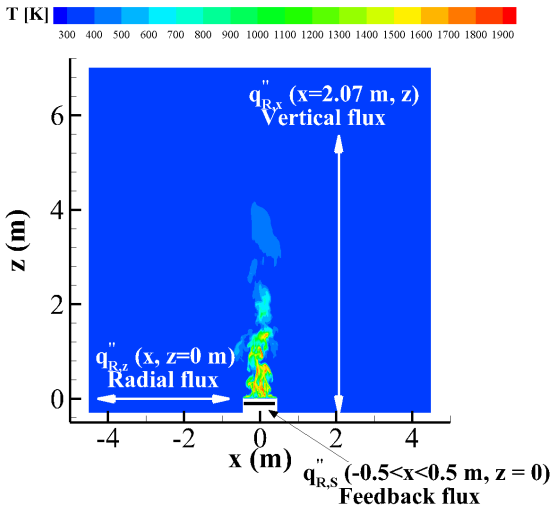

Figure 1: A shematic diagram of the computational domain and the locations of the radiative heat flux distributions.

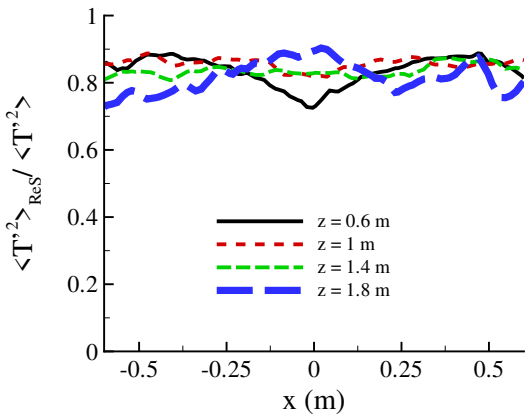

Figure 2: Radial evolution of resolved-part of temperature variance at different heights.

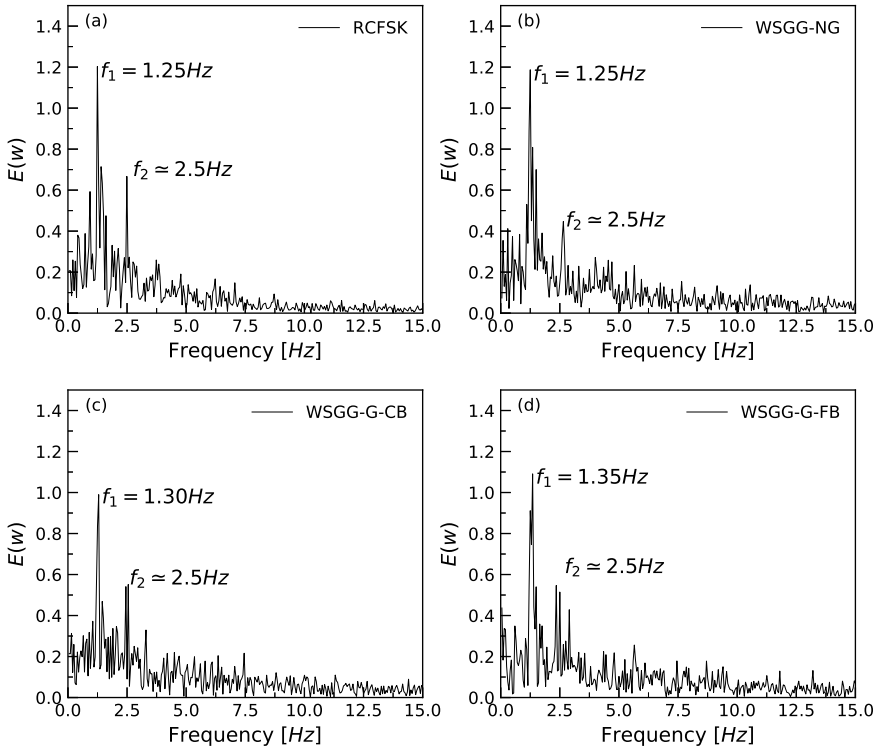

Figure 3: Predicted Power Spectrum Density from axial velocity along the flame axis at z = 0.6 m

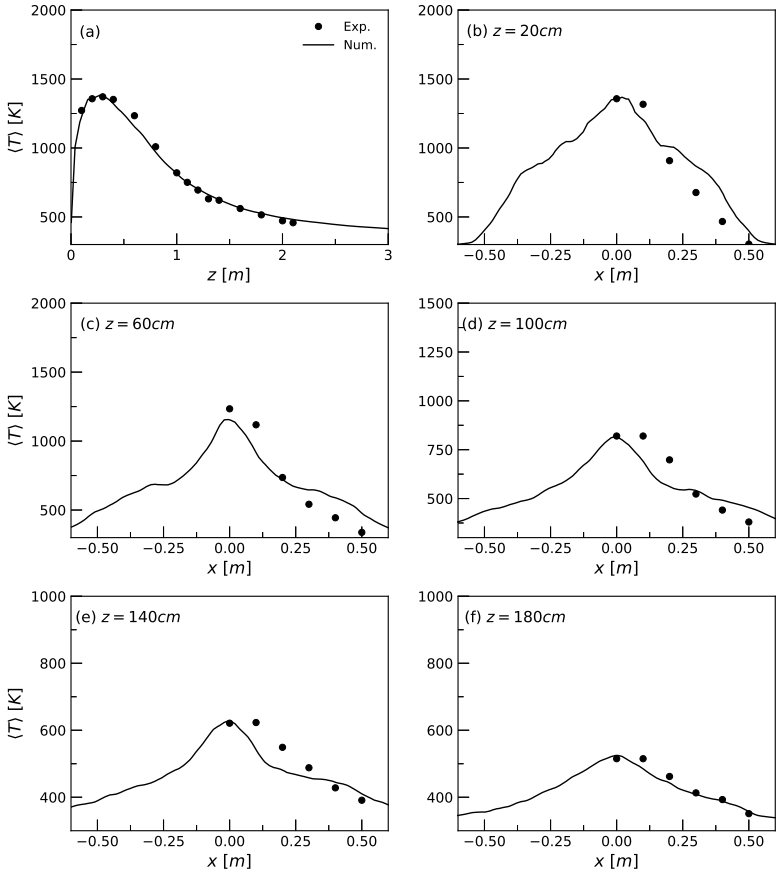

Figure 4: Axial and radial profiles of mean temperature. The experimental data are taken from Ref. [44].

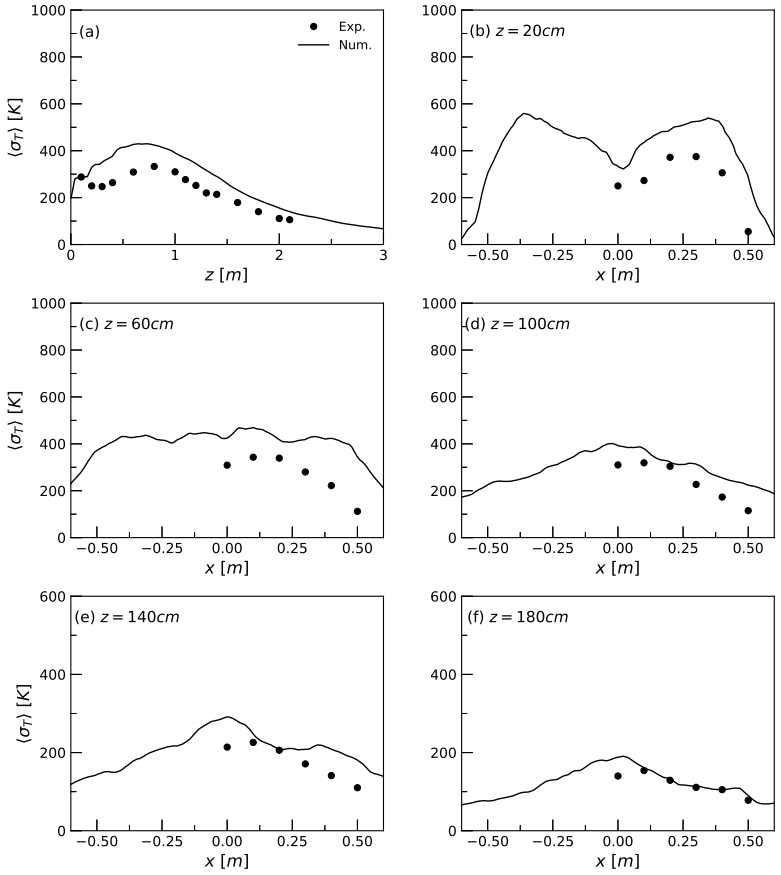

Figure 5: Radial profiles of rms values of temperature fluctuations at different heights. The experimental data are taken from Ref. [44].

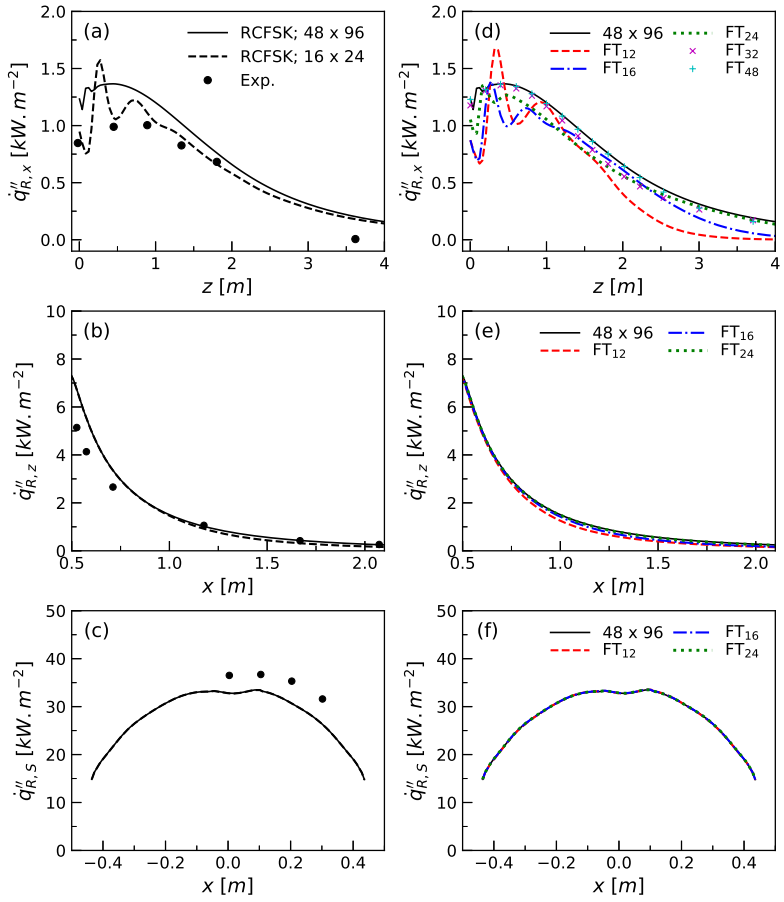

Figure 6: Effects of angular meshes on radiative heat fluxes. The location of the distributions are described in Fig. 1. a) and d) Vertical distribution at a distance r=2.07 m from the pool axis, b) and e) radial distribution outside the burner along the plane of the burner rim. The radial distance is measured from the pool center, and c) and f) feedback toward the fuel surface. The experimental data in the diagrams a) and b) are taken from Sung et al. Ref. [44] whereas those in diagram c) are taken from [65]. All the simulations were obtained with the RCFSK. The diagrams a), b) and c) investigate the effects of the uniform meshes whereas the diagrams d), e), and f) those of the FT_n FVM angular discretizations.

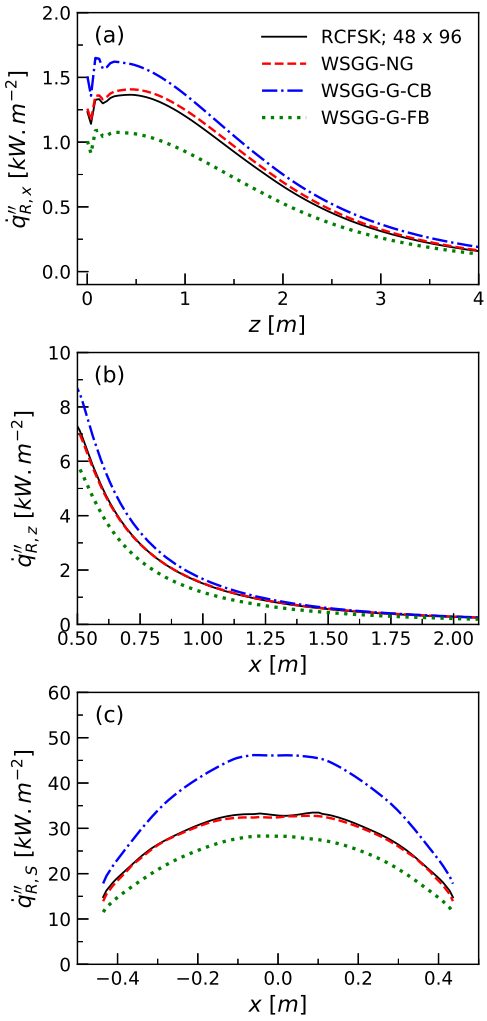

Figure 7: Effects of gas radiative property models on raditive heat flux. The location of the distributions are described in Fig. 1. a) Vertical distribution of radiative flux at a distance r = 2.07 m from the pool axis, b) radial distribution outside the burner along the plane of the burner rim. The radial distance is measured from the pool center, and c) radiative feedback toward the fuel surface. These radiative fluxes are computed in frozen field analysis using the FVM 48 × 96 angular discretization.

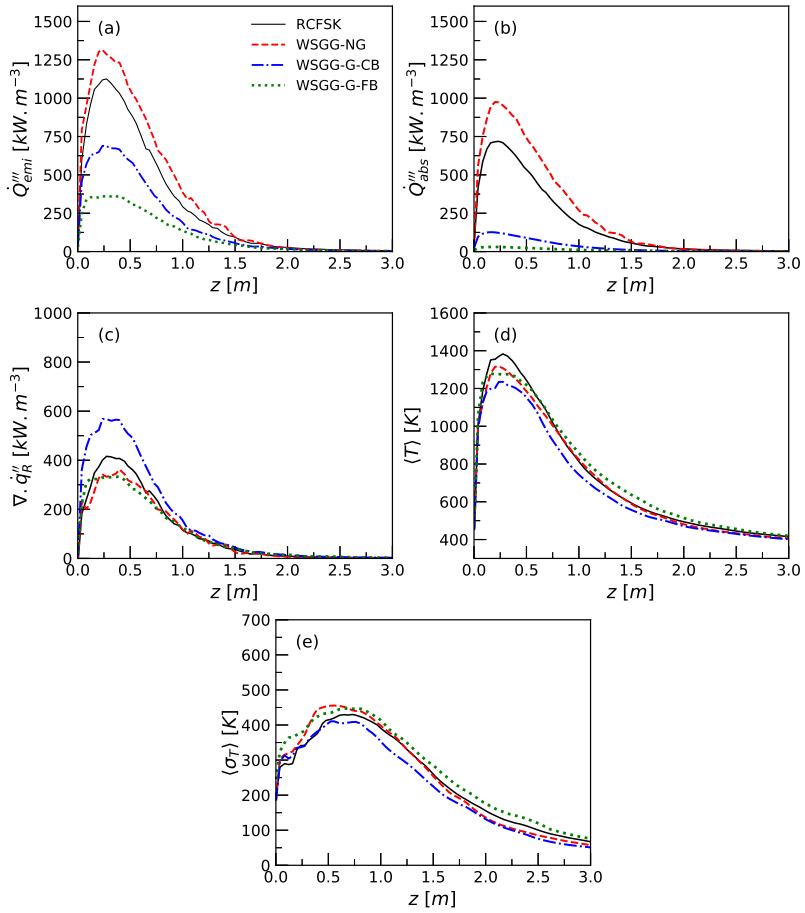

Figure 8: Effects of radial property models on the axial distributions of: a) emission term, b) absorption term, c) divergence of the radiative flux, d) mean temperature, and e) rms values of temperature fluctuations. These radiative fluxes are computed in frozen field analysis by using the FVM 48 $\times$ 96 angular discretization.